

Reconfigurable Magnetic Slime Robot: Deformation, Adaptability, and Multifunction

Mengmeng Sun, Chenyao Tian, Liyang Mao, Xianghe Meng, Xingjian Shen, Bo Hao, Xin Wang, Hui Xie,* and Li Zhang*

Magnetic miniature soft-bodied robots allow non-invasive access to restricted spaces and provide ideal solutions for minimally invasive surgery, micromanipulation, and targeted drug delivery. However, the existing elastomer-based (silicone) and fluid-based (ferrofluid or liquid metal) magnetically actuated miniature soft robots have limitations. Owing to its limited deformability, the elastomer-based small-scale soft robot cannot navigate through a highly restricted environment. In contrast, although fluid-based soft robots are more capable of deformation, they are also limited by the unstable shape of the fluid itself, and are therefore poorly adapted to the environment. In this study, non-Newtonian fluid-based magnetically actuated slime robots with both the adaptability of elastomer-based robots and reconfigurable significant deformation capabilities of fluid-based robots are demonstrated. The robots can negotiate through narrow channels with a diameter of 1.5 mm and maneuver on multiple substrates in complex environments. The proposed slime robot implements various functions, including grasping solid objects, swallowing and transporting harmful things, human motion monitoring, and circuit switching and repair. This study proposes the design of novel soft-bodied robots and enhances their future applications in biomedical, electronic, and other fields.

far, most magnetically actuated soft-bodied robots have been fabricated from soft elastomers mixed with hard magnetic particles.^[26–43] Such elastomer-based soft robots perform multiple movement modes,^[26–28] adapt to complex interface environments,^[31,32] and enter confined spaces for robotic manipulation applications.^[33–35] However, the functionality of elastomer-based soft robots is limited by their pre-designed shapes and cannot be reconfigured in situ. Moreover, elastomer-based soft robots possess limited deformation capabilities and cannot pass through narrow spaces that are significantly smaller than their dimensions.

In contrast, recent studies have demonstrated that small fluid-based robots, such as those based on liquid metal or ferrofluid,^[44–50] behave more gently and softly. Fluid-based soft robots exhibit better deformability than elastomer-based soft robots owing to their fluid flow properties that allow them to easily pass through extraordinarily narrow and restricted


1. Introduction

Miniature robots that respond to external stimuli have the advantage of being less invasive and more accessible,^[1–6] making them exciting candidates for biomedical applications^[7–12] such as targeted drug delivery,^[13,14] minimally invasive surgery,^[15] and cell transplantation.^[16,17] Owing to its safety, precision, and fast response, an external magnetic field is a promising choice for actuating small-scale robots.^[18–25] Thus

spaces and avoid damaging surrounding biological tissues.^[51,52] For instance, by constructing an electromagnet array, an intelligent deformable and cooperative ferrofluid-based soft robot that could pass through 1.5 mm diameter narrow channels and perform various functions^[53] was constructed. In addition, researchers have also realized the control of electric circuits and fluid pumping using liquid-metal-based soft robots.^[54] However, ferrofluid- and liquid metal-based robots require very demanding operating environments; for instance, oil-based

M. Sun, B. Hao, X. Wang, L. Zhang
Department of Mechanical and Automation Engineering
The Chinese University of Hong Kong
Hong Kong SAR 999077, China
E-mail: lizhang@cuhk.edu.hk

C. Tian, L. Mao, X. Meng, X. Shen, H. Xie
State Key Laboratory of Robotics and Systems
Harbin Institute of Technology
2 Yikuang, Harbin 150001, China
E-mail: xiehui@hit.edu.cn

 The ORCID identification number(s) for the author(s) of this article can be found under <https://doi.org/10.1002/adfm.202112508>.

DOI: 10.1002/adfm.202112508

L. Zhang
Department of Surgery
The Chinese University of Hong Kong
Hong Kong SAR 999077, China

L. Zhang
CUHK T Stone Robotics Institute
The Chinese University of Hong Kong
Hong Kong SAR 999077, China

L. Zhang
Chow Yuk Ho Technology Center for Innovative Medicine
The Chinese University of Hong Kong
Hong Kong SAR 999077, China

L. Zhang
Multi-Scale Medical Robotics Center
Hong Kong Science Park, Shatin NT, Hong Kong SAR 999077, China

ferrofluids require hydrophilic surfaces surrounded by water-based solutions to maintain the shape of the spherical droplets without adhering to the substrate,^[53] whereas liquid metals require alkaline or acidic solutions to preserve the form of spherical droplets without adhering to the substrate.^[55,56] Therefore, it is necessary to combine the characteristics of large deformations of liquid-based robots with the complex interface adaptability of elastomer-based robots to create novel soft robots.

To satisfy this demand, we propose multifunctional magnetic slime robots with large deformations and adaptability. We report the fabrication process of a magnetic slime and its fundamental mechanism of shape transformation. In comparison with existing elastomer-based soft robots, our proposed slime robot has better deformability, for instance, through narrow pipes (1.5 mm) and complex maze environments. In addition, when compared to existing fluid-based soft robots, the slime robot has greater environmental adaptability, allowing movement not only in two-phase fluids but also in air, and even on various surfaces such as hydrogel, metallic, and plastic surfaces. Thereafter, we demonstrate that this slime robot can have multiple reconfigurable functions, such as grasping and delivering objects through the curling mode and wrapping and transporting harmful things through the endocytosis mode. In addition, the ability to self-heal and conduct electricity allows the slime robot to be used as an electrical device, for instance, as a piezoresistive strain sensor to monitor human movement and as a circuit control switch or circuit breaker repair agent. Thus, our proposed non-Newtonian fluid-based robot with a large deformation, reconfigurability, self-healing, and conductivity is expected to be of great value in wearable devices and biomedical applications.

2. Results and Discussion

2.1. Preparation and Characterization of the Magnetic Slime

The preparation scheme of the magnetic slime is illustrated in **Figure 1a**, where magnetic particles (NdFeB) and borax were sequentially added to a polyvinyl alcohol (PVA) solution to obtain the magnetic slime. The inset in **Figure 1a** shows the critical reactions necessary for the formation of the magnetic slime. Magnetic slime is formed primarily through the interaction of tetrafunctional borate ions with the $-OH$ group of PVA, where tetrafunctional borate ions are generated through the hydrolysis of borax. Notably, magnetic slime consists of >90 wt% water, implying that it is essentially a hydrogel (**Figure 1b**). As shown in (**Figure 1c**), scanning electron microscopy (SEM) images indicate that the microstructure of the magnetic slime is a 3D porous network of magnetic particles cross-linked with immobilized polymers. The porous structure is favorable for the extensibility and fast response of the magnetic slime. In addition, we investigated the cytotoxicity of the slime. As shown in **Figure S1A**, Supporting Information, at concentrations up to $400 \mu\text{g mL}^{-1}$, non-magnetic slime is non-toxic to NIH 3T3 cells, indicating its excellent biocompatibility. However, NdFeB particles are toxic, thus making the magnetic slime (NdFeB: 30%) non-biocompatible. Therefore, the NdFeB

microparticles were coated with SiO_2 via the Stober method. Transmission electron microscopy images demonstrated that the NdFeB microparticles were coated with a layer of 35 nm SiO_2 (**Figure S1B**, Supporting Information). Subsequently, they were added to the PVA solution to prepare the magnetic slime. Cytotoxicity tests showed that the $400 \mu\text{g mL}^{-1}$ magnetic slimes prepared using NdFeB@ SiO_2 were not toxic to cells.

Magnetic slime has both active and passive deformation capabilities, and its shape can be changed by altering the external magnetic field or it can be adapted to environmental boundaries using rheological properties. The rheological and magnetorheological properties of the slime were measured using a rheometer (Anton Paar MCR302) with a 25 mm parallel plate setup. A dynamic strain sweep ranging from 0.1% to 100% at $\omega = 10.0$ Hz was first performed, and the storage modulus (G') was recorded to define the linear viscoelastic region (LVR) in which the storage modulus is independent of the strain amplitude (**Figure 1d**). A strain of 1.0% was selected in subsequent oscillation tests to ensure that the dynamic oscillatory deformation of each sample was within the LVR. **Figure 1e** shows the changes in the storage (G' , solid symbols) and loss moduli (G'' , hollow symbols) as a function of angular frequency for non-magnetic slime (NdFeB: 0%) and magnetic slime (NdFeB: 50%). Both slimes are in a solid state, with the storage modulus exceeding the loss modulus over the entire frequency range. It is observed that the presence of NdFeB microparticles raises the moduli and enhances the elastic response of the slime. In addition, **Figure 1f** shows the dependence of G' on the magnetic field at a fixed strain amplitude (0.2%) and angular frequency (6 rad s^{-1}). The change in storage modulus for the magnetic slime is significant in increasing the magnetic field strength, indicating a significant magnetorheological effect. Applying a magnetic field enhances the mechanical properties of the magnetic slimes owing to the magnetic dipole–dipole forces. Magnetic-field-dependent dynamic viscoelasticity is mainly attributed to the interaction between adjacent particles when they are magnetized. Such interactions condense the polymer chain and make the structure more rigid. The magnetorheological effect causes magnetic slimes to exhibit tunable stiffness by applying a magnetic field. Therefore, it is possible to control the stiffness of the magnetic slime to adapt it to different working environments. In **Figure 1g**, we first investigate the active deformation behavior of magnetic slimes, which can deform into complex shapes, such as circles, hexagons, and rings, under the configured magnetic field. Both experiments and simulations reveal that the morphology of the magnetic slime is similar to that of the permanent magnet at the bottom because the unmagnetized magnetic particles in the slime tend to move to the position with the lowest magnetic field strength.^[53] This allows the magnetic slime to change its morphology depending on the needs of different tasks. **Figure 1h** shows that the magnetic slime can be driven by a permanent magnet (NdFeB) and stretched more than seven times its original length along the direction of the magnet motion. At $t = 0$ s, a magnetic slime with a diameter of 9 mm was placed on a polymethylmethacrylate substrate, and a circular permanent magnet with a diameter of 20 mm and height of 10 mm was set at a distance of 4 mm below the substrate. As the circular permanent magnet moved at a speed of 2 mm s^{-1} , the slime started to elongate and stretched

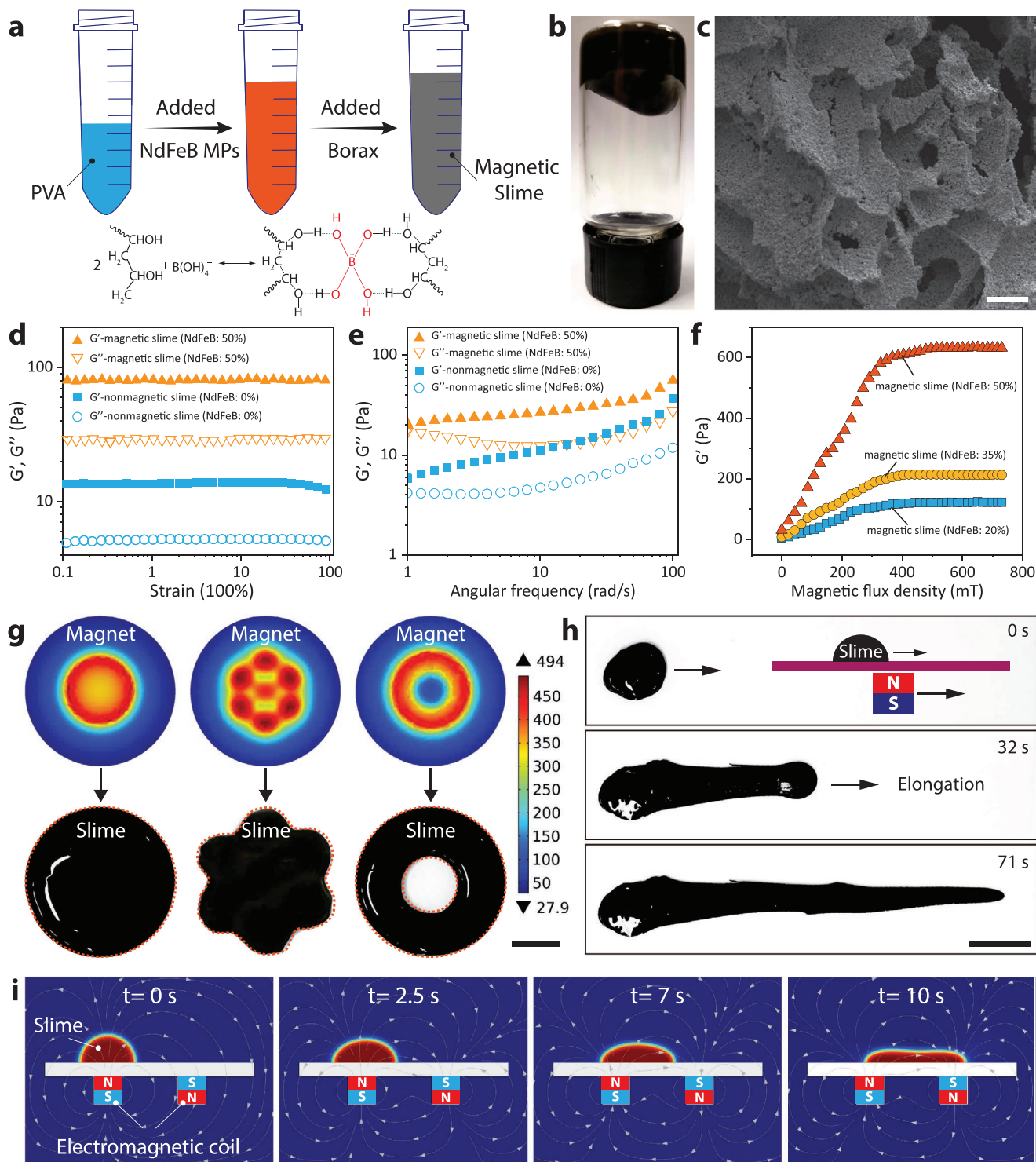


Figure 1. Synthesis process and deformability of magnetic slime. **a)** Schematic diagram of the magnetic slime fabrication process. Inset illustrates the crosslinking reaction between PVA and a tetrafunctional borate ion. **b)** Image of the magnetic slime. **c)** SEM images of the freeze-dried unmagnetized slime. Scale bar, 100 μm . **d)** Strain dependence of G' and G'' for non-magnetic slime and magnetic slime, respectively, measured at $\omega = 10.0$ Hz. **e)** Frequency dependence of G' and G'' for non-magnetic slime and magnetic slime, respectively, measured at a strain of 1.0%. **f)** Magnetic field dependence of the storage modulus G' of magnetic slime with varying weight percentages of the NdFeB particles measured at 0.2% deformation and oscillation frequency of 6 rad s^{-1} . **g)** Programming complex shapes of the magnetic slime using ferromagnets in disk-, hexagon-, and ring-shapes. The simulation results demonstrate the magnetic field distribution in the plane 2 mm above the magnet. Scale bar, 15 mm. **h)** Experimental frames of the stretchable behavior of the magnetic slime. Scale bar, 10 mm. **i)** Simulation of controlled deformation behavior of magnetic slime.

to 60 mm after 71 s. The elongation process of the slime was reproduced using COMSOL Multiphysics software (Figure 1i; Movie S1, Supporting Information). In addition, the ability to deform allows the slime to elongate, whereas the friction with the interface and the configuration of the magnetic field allow the slime to remain locked in the path travelled. As shown in Figure S2, Supporting Information, the magnetic slime can actively deform into the shape of “CUHK” along the direction of motion of the permanent magnet.

2.2. Environmental Adaptability

The passive and active deformation capabilities of magnetic slimes give them a remarkable advantage, not only for adapting to complex terrain environments but also for entering confined spaces in a controlled manner while maintaining their mobility and integrity. The shape-shifting nature allows the slime to adapt to changing external environments to satisfy the demands of multitasking. As illustrated in Figure 2a, under the control of a magnetic field, the slime can navigate freely through various terrains such as narrow channels, confined tubes, complex mazes, and uneven substrates (Movie S2, Supporting Information). First, an array of channels with diameters of 6, 4.5, 3, and 1.5 mm were prepared to test the deformation ability of the magnetic slime. According to the experimental results, although it took a long time (≈ 180 s) for the magnetic slime to pass through the 1.5 mm diameter channel, eventually, the slime could successfully pass through each channel in turn. Subsequently, we demonstrated that 1 mL magnetic slime can flow smoothly in a liquid-free tube with an inner diameter of 5 mm. Deformability allows the slime to negotiate the curved tube structure quickly and stretch its shape along the direction of movement within the tube. In addition, a maze with varied inner diameters (minimum gap: 1.5 mm) and complex branches was also prepared to demonstrate the deformability and controllability of the slime. Finally, we demonstrate that slimes can migrate over uneven terrain with a width of 6.28 mm and height of 3 mm. The magnetic slime can maneuver unobstructedly over multiple terrains by actively and passively changing its shape, dramatically reducing its damage to the surrounding environment and expanding its application scenarios.

To achieve optimally controlled deformation of the magnetic slime, we systematically investigated the aspect ratio of slime when varying the content of magnetic particles and the strength of the applied magnetic field. As shown in Figure 2b, the aspect ratio of the magnetic slime deformation is proportional to the magnetic particle content when the applied magnetic field is the same. Under an external magnetic field, the increase in the magnetic powder content dramatically enhances the magnetic response of the slime, causing it to be subjected to a more significant deformation force. In addition to the magnetic particle content, the outer magnetic field strength also affects the deformation behavior of the magnetic slime. Figure 2c shows that the deformation ability of the magnetic slime is positively correlated with the strength of the external magnetic field. The motion behavior of the internal particles of the slime is determined by the magnetic field strength that affects its overall deformation properties. To characterize the

mobility of the magnetic slime in a restricted environment, we also investigated the minimum diameter of the tube through which the slime could pass when the strength of the external magnetic field was varied. The experimental results demonstrate that the minimum diameter of the channel through which the slime can pass is 1.5 mm for a fixed content of magnetic particles and slime volume. The minimum diameter of the tube through which it can pass increases as the external magnetic field strength decreases (Figure 2d). In addition, we systematically compared the deformability of ferrofluid droplet, magnetic liquid metal, and magnetic slime robots under equal magnetic field strength. Ferrofluids with dynamic viscosities of 8 mPa s (EMG 901; Ferrotec Corporation) were used in this experiment, and the deformation environment was water. In addition, a magnetic liquid metal robot was constructed using a previously reported method,^[54] and its deformation environment was a 2 mol L⁻¹ hydrochloric acid solution. As shown in Figure S3A, Supporting Information, under a low magnetic field strength, the deformation ability of the ferrofluid droplet robots is the best; however, as the magnetic field strength increases, it becomes difficult for the ferrofluid droplet robots to remain intact. The maximum elongation length increased linearly as the magnetic field strength increased for the slime and liquid metal robots. Under equal magnetic field strength, the elongation length of the slime robot was greater than that of the magnetic liquid metal robot. In addition, we compared the maximum elongation lengths of ferrofluid droplet, magnetic liquid metal, and slime robots with equal volumes. The results demonstrate that the elongation of the slime robot was the largest when the three volumes were equal (Figure S3B, Supporting Information).

In addition to its excellent terrain adaptability, magnetic slimes can move across multiple interfaces, which is impossible for conventional liquid-based robots. The structure of the slime gives it the adaptability of an elastomer-based robot and the ability to deform substantially as a liquid-based robot, but without the disadvantages of either form. Thus far, the movement of liquid-based soft robots, such as ferrofluids or liquid metals, requires hydrophilic interfaces or alkaline solutions, which significantly limits their application. However, our proposed magnetic slime can be adapted to a wide range of substrates. We prepared a total of eight commonly used substrates, including hydrogel, metal, plastic, glass, silica, silicon, polydimethylsiloxane, and paper substrates, and cut them into 10 cm \times 10 cm pieces. As illustrated in Figure 2e, when actuated by a permanent magnet, a 500 μ L slime can follow the trajectory of “SLIMEBOT” on these substrates. In addition to the demonstrated controlled deformation behavior of slime in air, it can also work stably underwater and meet the needs of various tasks (Figures S4 and S5, Supporting Information). The deformation ability of the slime underwater is better than that in air, which takes only 50 s to pass through the narrow channel with a diameter of 1.5 mm because the liquid environment dramatically reduces the adhesion between the slime and the channel (Movie S3, Supporting Information). The PVA component endows the slime with a self-adhesive ability. As shown in Figure S6A, Supporting Information, the hydroxyl groups in the molecular chain of PVA combined with water molecules, resulting in strong hydrogen bonds. When the

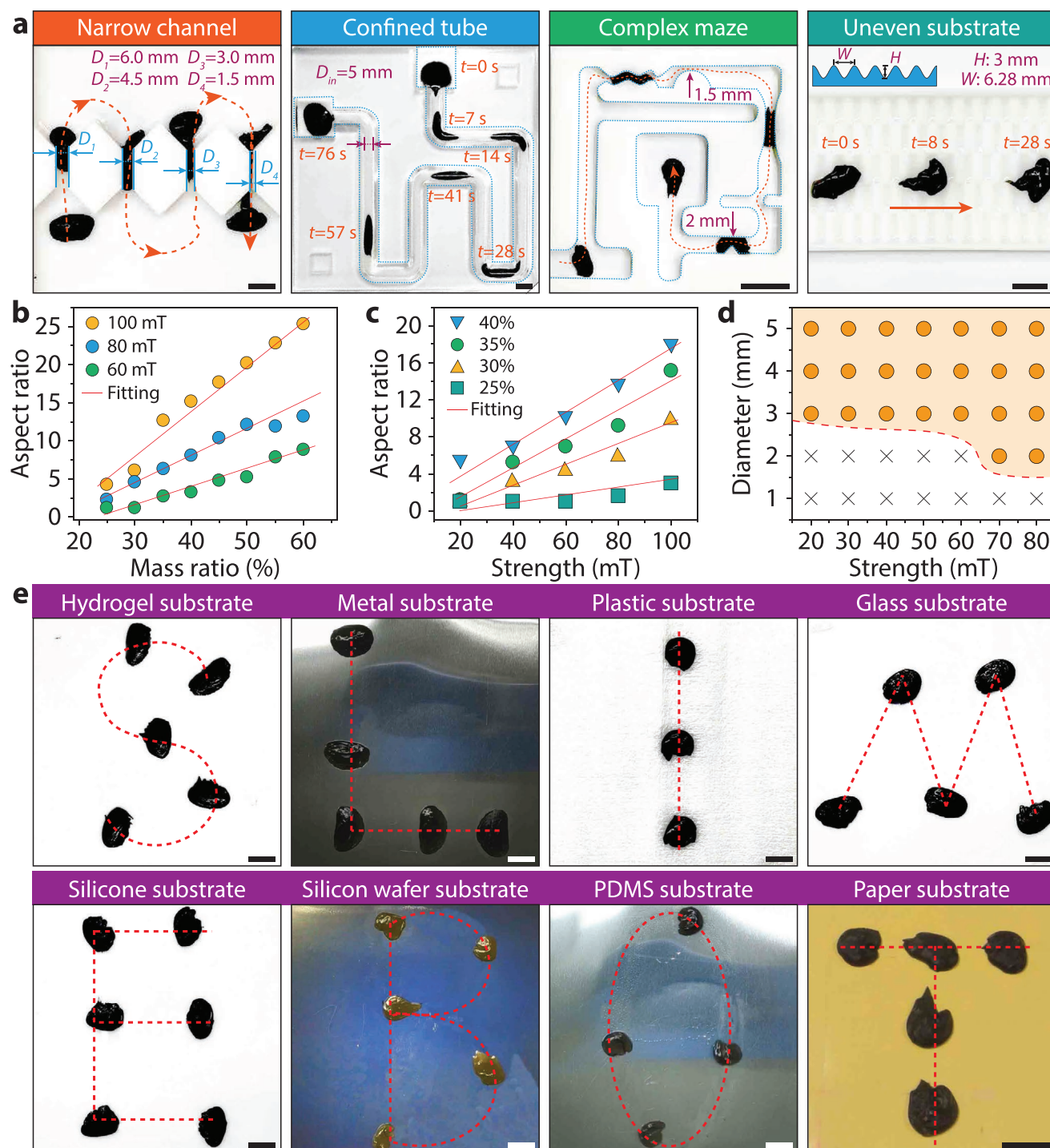


Figure 2. Environmental adaptability analysis. a) Overlapped sequential snapshots of videos show that the magnetic slime is actuated to navigate through the channel, tube, maze, and uneven surfaces in air. b) The deformation ability of magnetic slime is a function of the content of the inner magnetic particles. c) Relationship between the strength of the permanent magnet and deformation ability of magnetic slime with varying magnetic power content. d) Minimum diameter of the magnetic slime that can pass through the thin tube versus the magnetic field strength. e) Overlapped sequential snapshots of videos demonstrate that the magnetic slime is actuated along the “S”, “L”, “I”, “M”, “E”, “B”, “O”, and “T” trajectories on varying substrate surfaces in air. Scale bars, 10 mm.

slime fills the gap and is in complete contact with the substrate, it also adheres to the substrate through van der Waals forces. To further understand the adhesion properties of slime,

we experimentally investigated the peeling strength between the slime and the substrate (Figure S6B, Supporting Information). As shown in Figure S6C, Supporting Information, the

experimental results demonstrate that paper has the highest bond strength that decreases with increasing magnetic particle content. This is mainly due to the better water absorption effect of the paper and the rough surface where the slime can diffuse into the micropores and be retained as a residue during peeling. The hydrogen bonding between the PVA molecular chains enhances adhesion during the tearing of the material when the bonding force of the hydrogen bond is greater than the aforementioned van der Waals force. Furthermore, magnetic particles can decrease the slime adhesion properties because they prevent the hydroxyl groups in the PVA molecular chain from combining with water molecules. This adhesion property reduces the deformation rate and overall motion speed; however, the driving magnetic field can overcome it,

preventing it from affecting the final deformation and reachable range. The adaptability of slime to external environments allows it to meet multitasking needs such as micromanipulation and biomedical applications.

2.3. Controlled Manipulation

In addition to adapting to various complex terrains based on their rheological properties, slimes can also utilize reconfigurability to achieve flexible manipulation. **Figure 3a** shows that slimes can perform object grasping using the curling mode after being elongated (Movie S4, Supporting Information). The mechanism of the curling mode is illustrated in Figure S7,

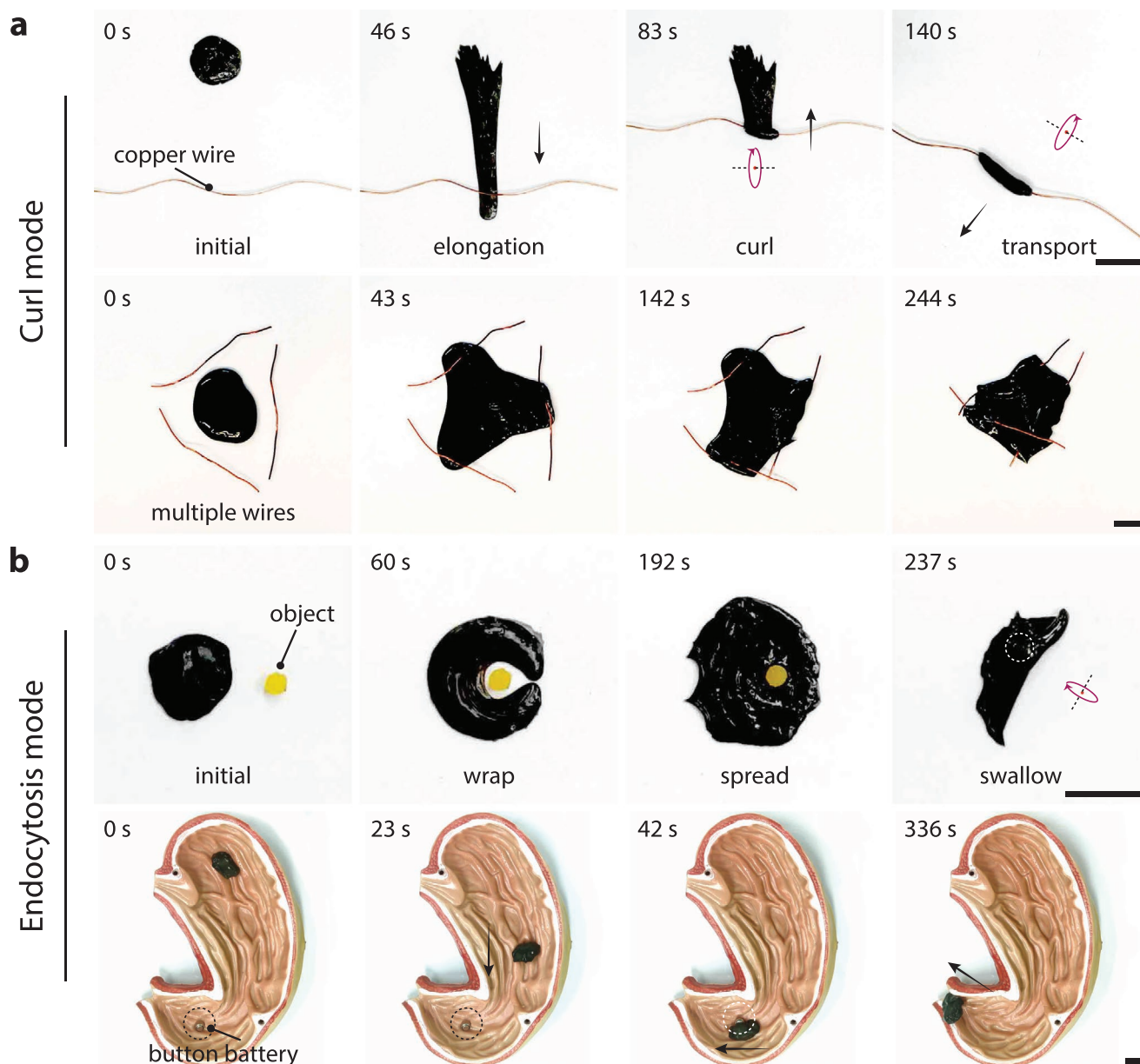


Figure 3. Multimodal manipulation. a) Slime grasps a single target object (above) and multiple target objects (below) in curling mode. b) Slime grasps target objects in open environment (above) and complex restricted environment (below) in endocytosis mode. Scale bars, 10 mm.

Supporting Information. At $t = 0$ s, the magnetic slime actuated by the permanent external magnet began to stretch. After 46 s, the slime elongates to the bottom of the target object. During the elongation process, the magnetic particles in the slime are magnetized by a permanent external magnet and maintain a consistent magnetization direction. Because slime exhibits non-Newtonian behavior leading to limited dimensional stability,^[57] the orientation of internal magnetic particles with remanent magnetism does not change for a short time when the permanent external magnet is withdrawn. At this time, if a rotating magnetic field is applied, the elongated magnetic slime starts to curl and hook the target object ($t = 83$ s). Finally, driven by the rotating magnetic field, the slime continues to curl until it eventually wraps the target object completely and can carry it for rolling motion ($t = 140$ s). Furthermore, the magnetic slime can grasp multiple target objects simultaneously using its deformation characteristics, as shown in Figure 3a. When the manipulated object is present in all three directions, the slime can extend its tentacles in three directions, such as an octopus arm ($t = 43$ s). Thereafter, an external rotating magnetic field is applied in sequence, and the three tentacles of the slime begin to curl sequentially. Finally, the three target objects were grasped using the curl mode (Movie S4, Supporting Information). The curl operation mode can help accomplish the grasping function for long-range restricted environmental species.

Owing to its shape-shifting property, the slime can also grasp and transport objects through endocytosis. As illustrated in Figure 3b (above), the slime can swallow the target object through wrapping, spreading, and curling, consecutively (Movie S5, Supporting Information). At $t = 0$ s, the magnetic slime begins to deform under the action of the bottom-ring-shaped permanent magnet. The circular slime gradually becomes C-shaped when the ring-shaped permanent magnet is tilted, and moving the permanent magnet can induce the slime to enclose the target object ($t = 60$ s). Thereafter, the C-shaped slime becomes a ring when the ring-shaped permanent magnet is placed parallel to the operating surface. Subsequently, the permanent magnet was continuously moved outward in a reciprocal manner to spread the slime on a flat surface ($t = 192$ s). As the slime expands, the permanent magnet magnetizes the magnetic particles in the slime. Finally, the slime curls under a rotating magnetic field and swallows the target object placed on top of it ($t = 237$ s). When an object is swallowed by the slime, it is completely isolated from the external environment, which facilitates the capture of dangerous objects. For instance, magnetic slime can be used in clinical interventions for button battery ingestion, which seriously endangers the life of the patient. We simulated human ingestion by sandwiching button batteries between the lining of the large intestine of a pig. After 30 min, it caused severe damage to the lining of the intestine (Figure S8, Supporting Information). To reduce the risk of battery ingestion, magnetic slime is utilized and controlled by directing it to the injury site and thereafter to remove the stuck button battery through endocytosis (Figure 3b (below)). We prepared a simulated stomach model with the inner lining filled with folds. When the magnetic slime enters the stomach interior, it can move along the uneven inner wall, driven by an external magnetic field ($t = 42$ s). When the slime reaches the damage site, the button cell can be wrapped in the slime by

covering and curling to prevent further discharge and damage to the stomach lining (Movie S5, Supporting Information). In addition, the magnetic slime can transform into a crescent shape underwater and accomplish the collection and transport of solid spherical particles (Figure S9 and Movie S6, Supporting Information). Magnetic slime can also enter a complex and narrow maze environment by deforming and extending one end to achieve the target grasping operation (Figure S10, Supporting Information). Additionally, we quantitatively studied the relationship between the movement speed of the slime robot and the strength of the external magnetic field as well as the relationship between the curling rate and the strength of the external magnetic field. The experimental results demonstrated that the slime robot could reach the fastest speed of 30 mm s^{-1} under the drag of a spherical permanent magnet. When the magnetic field strength was less than 100 mT, the slime robot could not move as a whole. When a slime robot curls, the curling rate is proportional to the magnetic field strength. The higher the magnetic field strength, the faster the curling rate (Figure S11, Supporting Information). The magnetic slime system demonstrates curl and endocytosis modes of operation that can address multitasking needs.

2.4. Self-Healing and Electromechanical Analysis

The non-Newtonian fluid behavior of slime, combined with the magnetization character of its internal magnetic particles, endows it with remarkable deformability and reconfigurability. The damage and recovery of hydrogen bonds between its internal tetrafunctional borate ions and $-\text{OH}$ groups exhibit self-healing capabilities. This crosslinking was easily bound and dissociated dynamically at room temperature, thus exhibiting self-healing at room temperature. This occurs spontaneously without the help of external sources such as chemical reagents. Self-healing is mainly due to the sufficient mobility of the polymer chains within the slime and free tetrafunctional borate ions, allowing hydrogen bonds at the fracture interface to rapidly trigger the self-healing process in the absence of external stimuli.^[57] Two slime samples without the addition of magnetic particles were cut into four pieces and placed together to demonstrate their self-healing ability. The two samples were stained with green and blue dyes to distinguish the cut sites; thereafter, four small pieces of slime were joined together at intervals to begin healing. **Figure 4a** illustrates that the interface at the cut site is immediately reconnected (less than 1 s). The healed slime is well connected, maintains excellent plasticity, and withstands major strains even after being stretched to 8.6 times the original length without damage to the reconnected parts. As demonstrated in Figure 4b, a long strip of magnetic slime can eventually be healed into a circular shape after being cut into multiple pieces. First, at room temperature, the striped slime is cut into five small pieces; thereafter, driven by a magnetic field, the five slimes touch each other one by one, and finally, the magnetic slime completes the healing process (Movie S7, Supporting Information). In addition, in the face of puncture injuries, the slimes can still heal (Figure S12, Supporting Information). Slime possesses electrical conductivity properties. Thereafter, we clarified the time of self-healing

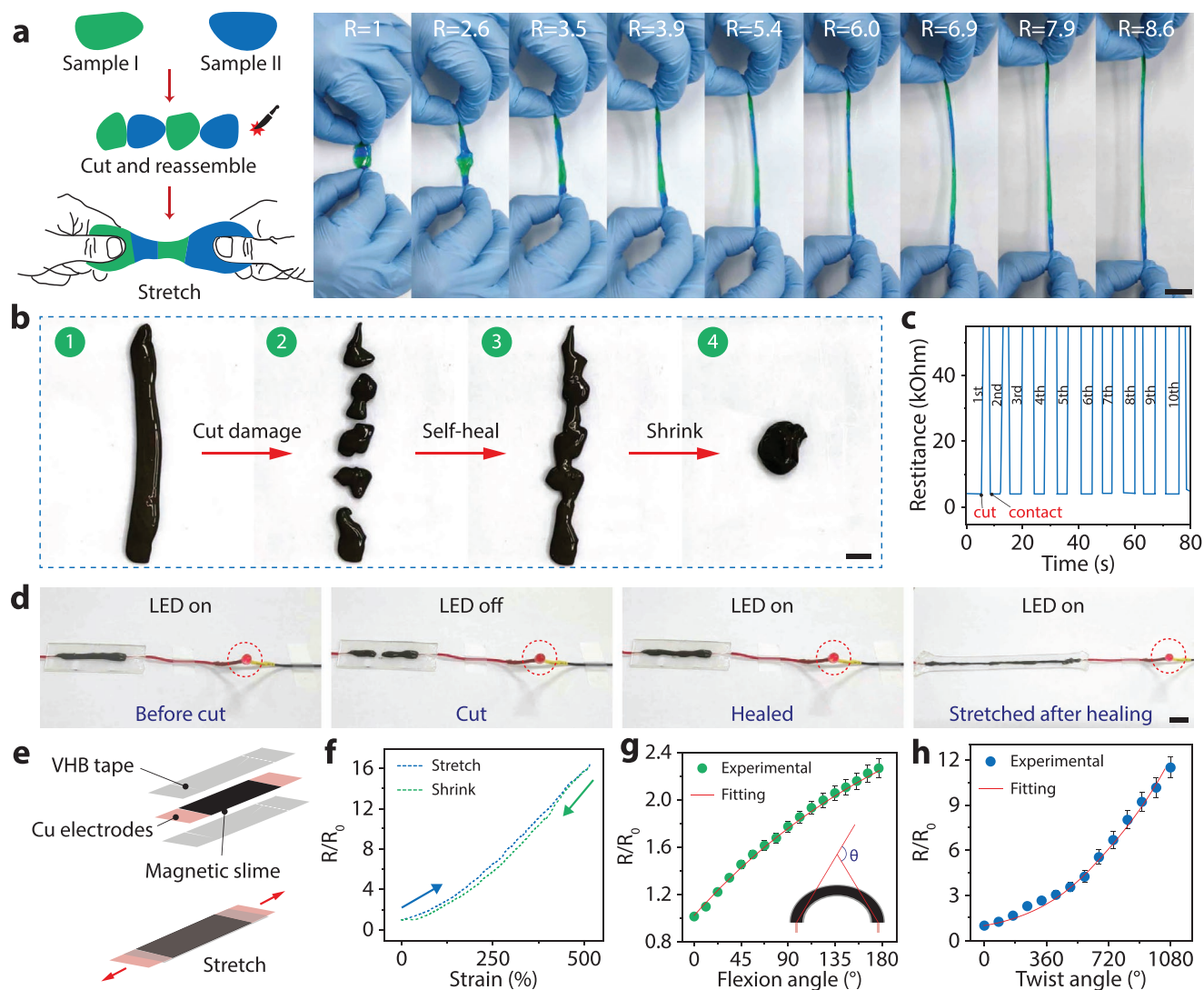


Figure 4. Electromechanical and self-healing analysis. a) The cut damage of slime samples (I and II) is healed in less than 1 s. The healed slime sample can withstand at least up to 8.6 times the stretch deformation, and the healed areas are as strong as the pristine areas. b) Sequence of images showing the healing process of magnetic slime. c) Cycling of the electrical self-healing capacity examination. d) Snapshots demonstrating the electrical healing capacity of magnetic slime. e) A layer of magnetic slime is sandwiched between two layers of VHB tape to create a piezoresistive strain sensor, which is thereafter connected to two Cu electrodes for tensile, bending, and twisting tests. f) Relative resistance of the magnetic slime as a function of strain. g) Normalized resistance versus bending angle ranging from 0° to 180° . The inset shows the definition of the bending angle. h) Variation of normalized resistance versus twist angle. Scale bars, 10 mm.

of the magnetic slime by measuring the resistance of the slime over time during the cutting–healing process. Figure 4c shows repeated cut–repair ten times at the same position of the magnetic slime. An open circuit is formed once the magnetic slime is completely cut and the resistance becomes infinite. When the broken parts were combined, the resistance dropped rapidly and returned to near the initial value within 1 s. Magnetic slime has significant and reproducible electrical repair properties and exhibits excellent self-healing efficiency during each cut and repair process (Figure S13, Supporting Information). Therefore, this self-healing ability may also cause electrical healing, that is, restored conductivity after the damage–healing cycle. Consequently, we connected magnetic slime to the circuit of the light-emitting diode (LED) bulb to test its electrical self-healing

capability (Figure 4d). As expected, when the magnetic slime was cut in half, the LED turned off immediately. After putting the two separated parts back together, the circuit heals quickly and the light intensity returns to the initial level.

The deformation and self-healing capabilities of magnetic slime allow it to be used as a motion sensor adapted to bending and dynamic mechanical environments. Considering the patterns of human motion (stretching, bending, and twisting), the electromechanical properties can be characterized. First, we encapsulated the magnetic slime between two pieces of VHB tape and connected the two ends using copper electrodes (Figure 4e). The VHB tape can create a strong connection between the magnetic slime and the copper electrodes to ensure repeatability during the test and to avoid evaporation

of water from the ion-conductive magnetic slime, which could alter the quality of the electromechanical signal. Figure 4f shows the relative resistance change versus strain, where the resistance increases with increasing strain. The relative resistance change was calculated as follows: $(R-R_0)/R_0 = \Delta R/R_0$, where R denotes the resistance at the tension state and R_0 denotes the resistance at the initial state. The relative resistance of the magnetic slime was 1600% at a strain of 500%, and this response was reproducible. In addition, a clear hysteresis exists within the large deformation (500%) stretch–release cycle. However, negligible hysteresis occurred during 100% strain (Figure S14, Supporting Information). In both cases, the initial resistance of the slime completely recovered after its release from the strain. The response of the magnetic lime-based strain transducer to deformation with bending and twisting was thereafter tested. Figure 4g reveals the change in resistance of the magnetic slime-based strain sensor as a function of the bending angle. The experimental results demonstrate that as the bending angle increased from 0° to 180°, the resistance increased from the original value to 220%. When the lime-based strain sensor is twisted, the variance in resistance obeys a parabolic equation for twist angles less than 540° (Figure 4h). However, at larger torsion angles (over 540°), the magnetic slime separates from each other around the torsion point, and the resistance increases rapidly. After three turns (1080°), the resistance increased from its value in the untwisted state to 1200%. In conclusion, the magnetic slimes can be modified into stable and repeatable piezoresistive strain sensors to maintain their operation in various mechanically demanding human body areas.

2.5. Applications of Magnetic Slime in the Electronic Field

Self-healing and deformable conductive slimes are promising tools for various electronic devices. First, the electroconductibility of the magnetic slime allows it to act as a circuit switch, as shown in the schematic in **Figure 5a**. A three-way circuit is fabricated, and processing each circuit will cause the red, blue, and yellow LED bulbs to light up (Movie S8, Supporting Information). In the initial state, the three LED bulbs were disconnected. Driven by an external magnetic field, the magnetic slime was controlled to light up the blue, yellow, and red LED bulbs in sequence. Interestingly, the slime can also transform into the shape of an octopus and turn on the three circuits simultaneously to light the three LED bulbs. In addition to acting as a circuit switch on a 2D plane, slimes can also be used to repair damaged circuits. Electronic devices may fail because of partial disconnection if they are corrupted by a long-term environment or are scratched by sharp objects. As illustrated in Figure 5b, the circuit repair process comprises three steps: stretching, spreading, and curling. The repaired circuit can function properly and light up the bulb (Movie S9, Supporting Information). As shown in Figure 5c, the magnetic slimes can achieve 3D open-circuit connections. In addition, sensors are an essential component of soft robots. Therefore, we explored the possibility of a slime robot acting as a sensor. We applied magnetic slimes encapsulated in VHB tape directly to the skin of the human body to detect bending and extension behavior, such as fingers, wrists, shoulders, and elbows. As shown in

Figure 5d, we monitored the variation in the resistance with respect to the bending angle of the index finger, wrist, shoulder, and elbow joints. When the index finger was repeatedly bent from the relaxed state (0°) to the bent state (90°) at a frequency of ≈ 1 Hz, the slime resistance changes monitored by the impedance analyzer exhibited a fast and repeated response to the finger motion. To detect wrist flexion, the resistance evolution of the sensor was measured at 45° and 90° bending angles, respectively. Interestingly, the resistance of the slime-based sensor increases with increasing bending angle (≈ 1.15 at 45° and ≈ 1.35 at 90°), thus allowing differentiation between different bending angles of the wrist joint. The sensor can also measure shoulder and elbow movements of the body separately. The presented sensor signal exhibited good stability during the cyclic measurements. Magnetic slime can use external deformation to obtain signals of human motion, and in the future, it may also use deformation signals to infer the position or stiffness of the robot. Theoretically, the magnetic slime robot combines motion and sensing, and will have a wider range of application scenarios in the future. In conclusion, this deformable, electrically conductive magnetic slime can be used in a number of applications, including wearable devices and soft robots.

3. Conclusions

We proposed reconfigurable multifunctional magnetic slime robots using spatiotemporally programmed external magnetic fields. In comparison with existing elastomer-based soft robots, our approach allows for greater deformation in these slime robots, which are capable of adapting to extremely constrained environments, such as passing through a narrow channel of 1.5 mm. In comparison with existing liquid-based robots, magnetic slime robots can adapt to complex interface environments, such as water or air, and can also achieve on-demand complex shape deformations and programmable behaviors such as curling operations. Various functions have been demonstrated for these slime robots, including navigation in narrow channels much smaller than their size, object capture operations via the curl or endocytosis modes, and circuit repair and controlled switching using their own conductive properties that can even be reconfigured as self-healing strain sensors for monitoring human motion. The widely applicable working environment of the presented magnetic slime robots, as well as their largely deformable, reconfigurable, self-healing, and conductive properties, make them promising for future applications in biomedical and wearable devices.

4. Experimental Section

Preparation of Magnetic Slime: First, 1 g of PVA was added to 20 mL of deionized water, and stirred at 90 °C for 3 h. Then 10 g of NdFeB powder (MQP-15-7, Magnequench, Inc.; average diameter 5 μ m) was added to the above solution, and the stirring was continued for 30 min under sonication. Meanwhile, 1 g of sodium tetraborate was dissolved with 20 mL of deionized water. Finally, the borax aqueous solution and the NdFeB/PVA solution were mixed with vigorous stirring at a volume ratio of 1:4 until a magnetic slime was obtained. The preparation method of magnetic slime with different magnetic particle content was similar,

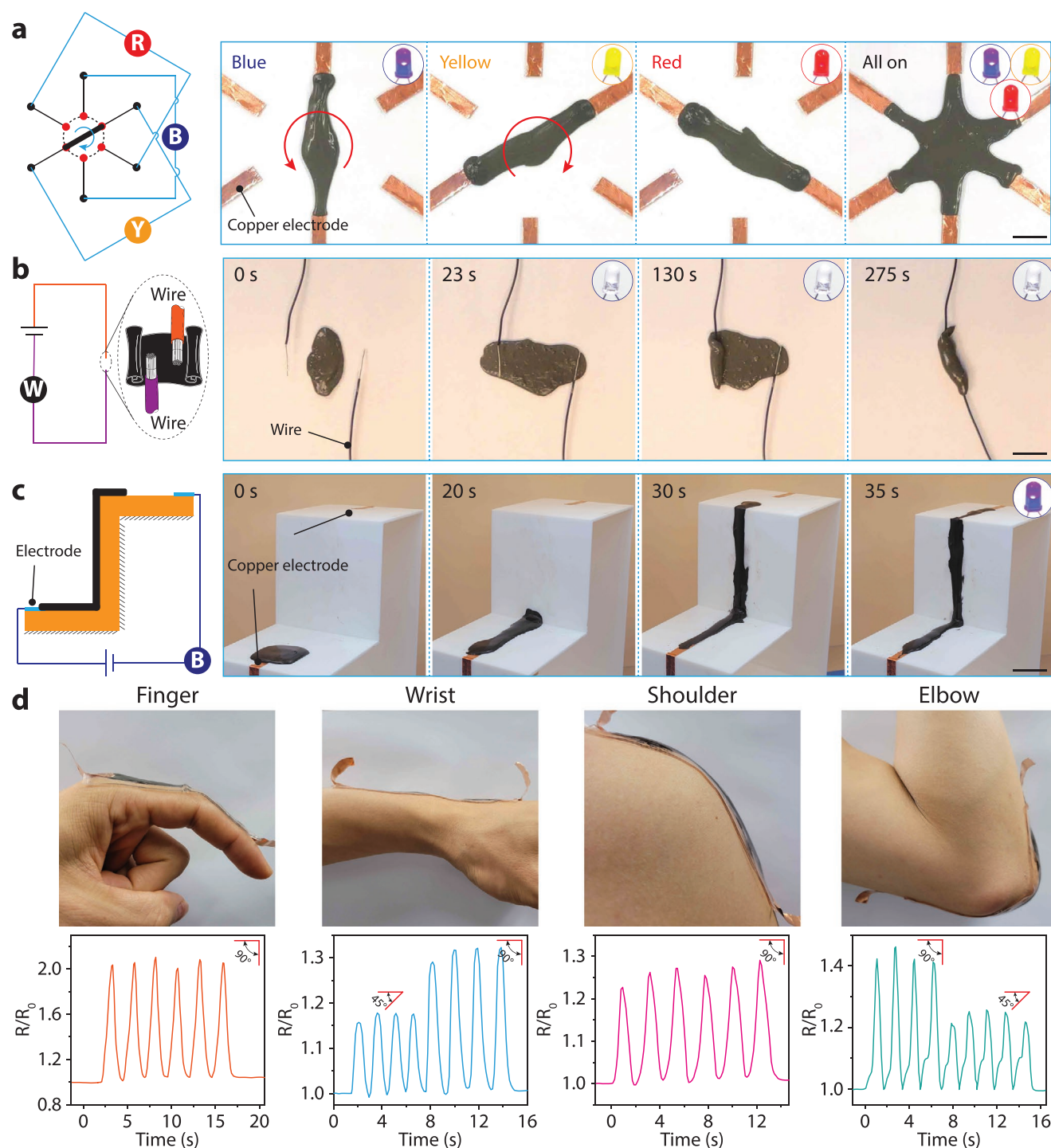


Figure 5. Human motion monitoring and circuit control. a) Experimental demonstration of a switch based on the magnetic slime. Inset illustrates the schematic of employing the magnetic slime as a microswitch. b) Schematic and corresponding experimental results of repairing broken circuit with magnetic slime. c) Schematic and corresponding experimental results of 3D circuit connections with magnetic slime. d) Movement in different parts of the human body causes changes in resistance. Images illustrating that the magnetic slime sensor can be firmly attached to the fingers, shoulders and elbows. Scale bars, 10 mm.

just change the ratio of NdFeB. However, the NdFeB particles were toxic, thus making the magnetic slime not biocompatible. Therefore, the NdFeB microparticles were coated with SiO_2 via the Stöber method.^[59] Typically, 100 mg of NdFeB microparticles were dispersed in 320 mL of ethanol, 80 mL of DI water, and 4 mL of ammonium hydroxide aqueous

solution (28%) via ultrasonic sonication for 15 min. Then, 0.2 mL of tetraethyl orthosilicate (98%) was slowly added into the mixture, followed by vigorous mechanical stirring for 6 h. The microparticles were then collected using a permanent magnet, washed with DI water five times, and finally dispersed in 80 mL of DI water.

Characterization: A scanning electron microscope (SEM, JEOL 7600F, Japan) was used to characterize the microstructure of the freeze-dried magnetic slime. The magnetic slime was dried by freeze drying (Scanvac CoolSafe 110⁻⁴ PRO 4lt freeze dryer) at −110 °C and 0.091 mbar before imaging. Rheometer (Malvern Kinexus lab+) was used to measure the rheological properties of slime.

Simulation and Computation: Commercial finite element software COMSOL Multiphysics was used to simulate the shape-changing of slime robot. The gravity was considered during the simulation, and all walls were defined as no-slip boundaries. Two electromagnetic coils of opposite polarity were placed at the two ends of the platform. The magnetic flux density norm of the left electromagnetic coil was equal to 200 mT during the whole simulation period, while the magnetic flux density of the right electromagnetic coil was equal to zero in the initial state, which gradually increased to 200 mT with time to simulate the process of a permanent magnet approaching the platform. The phase-field method was utilized to analyze the deformation of the slime robot surrounded by another fluid (in this simulation, the surrounding medium is water). The two-phase flow dynamic was governed by the Cahn–Hilliard equation, which was divided into two equations

$$\frac{\partial \phi}{\partial t} + \mathbf{u} \cdot \nabla \phi = \nabla \cdot \frac{\gamma \lambda}{\varepsilon^2} \nabla \psi \quad (1)$$

$$\psi = -\nabla \cdot \varepsilon^2 \nabla \phi + (\phi^2 - 1)\phi$$

where ϕ is the dimensionless phase field variable goes from −1 to 1 according to the fluid domain, \mathbf{u} is the fluid velocity, γ is the mobility, λ is the mixing energy density, and ε is the interface thickness parameter. The ψ variable is referred to as the phase-field help variable. The interface normal between two phases is then calculated as

$$\mathbf{n} = \frac{\nabla \phi}{|\nabla \phi|} \quad (2)$$

The magnetic force exerted on the slime robot was introduced by a volumetric force as shown in the following equation

$$\begin{cases} F_x = \left((H_x + M_x) \frac{\partial B_x}{\partial x} + (H_y + M_y) \frac{\partial B_z}{\partial y} \right) V_f, \\ F_y = \left((H_z + M_z) \frac{\partial B_x}{\partial x} + (H_y + M_y) \frac{\partial B_y}{\partial y} \right) V_f, \end{cases} \quad (3)$$

where V_f is the volume fraction of the slime robot. H_x and H_y are the relative components of magnetic field, M_x and M_y represent the magnetization, and B_x and B_y are the magnetic flux density in x and y directions.

In Vitro Cytotoxicity: To evaluate in vitro cytotoxicity, NIH 3T3 cells with a density of 2000 cells per well were seeded in a 96-well plate, followed by 12 h incubation in 100 μ L Eagle's Minimum Essential Medium with 10% fetal bovine serum. Then the medium was discarded, and 100 μ L fresh medium containing different concentrations of non-magnetic slime (NdFeB: 0%), magnetic slime (NdFeB: 30%), and magnetic slime (NdFeB@SiO₂: 30%) were added to the NIH 3T3 cells. Subsequently, these different samples were cocultured with the cells for 48 h. The MTS assay quantified cell viability. 10 μ L MTS solution was added to each well, followed by another 2 h incubation. Then nanoparticles were concentrated on the bottom with a permanent magnet, and the supernatant solution was transferred to a new 96-well plate. The absorbance was detected at 490 nm with a microplate reader. All of the tests were repeated three times.

Magnetic-Actuation Systems: The magnetic drive system in our work mainly consisted of a robotic arm, a stepper motor, and a spherical permanent magnet with a diameter of 20 mm. As shown in the Figure S15A, Supporting Information, the 3-degree-of-freedom robotic arm was loaded with motor-driven permanent magnets, and

the robotic arm could move to the targeted position autonomously encoded according to the task needs. Moreover, there was a step motor at the end of the robotic arm, and the motor can adjust the speed and direction of the permanent magnet on demand. Thus the whole system could generate a directional gradient magnetic field and a non-uniform rotating magnetic field. The magnetic field intensity distribution of a spherical permanent magnet is shown in the Figure S15B, Supporting Information, the magnetic field intensity of the surface of the permanent magnet was about 700 mT, and the magnetic field intensity at a distance of 10 mm from the permanent magnet was about 200 mT. In this work, the magnetic field strength to drive the magnetic slime robot through complex terrain, grasping and transporting objects, was about 200 mT and was marked in both the article and the videos. In addition, the magnetic slime robot was driven for circuit switching control, which was cooperatively controlled by two robotic arm systems, as shown in Figure S15C, Supporting Information. The qualitative comparison of the three magnetic soft materials in question 3 was also realized by the cooperative control of two manipulators carrying permanent magnets.

Calculation of Water Content: The water content (%) was calculated using the following equation^[58]

$$\text{water content (\%)} = \frac{W_i - W_d}{W_i} \times 100\% \quad (4)$$

where W_i is the initial weight of the slime before freeze drying and W_d is the weight of the freeze-dried slime.

Resistance Measurements: Resistance measurements during stretching with the CH Instruments Model 700E (CH Instruments, Inc.). A fixed AC excitation voltage of 2 V amplitude and 100 Hz was used for all measurements. And a sample with length, width, and height of 3, 2, and 0.1 cm, respectively were used for tensile testing. It was then sandwiched between two pieces of VHB tape (1 mm thick) and copper electrodes were attached at both ends (distance: 2 cm). Tensile tests (at a speed of 2 mm s^{−1}) were performed using a home-made linear actuator. In addition, the length and width of the samples used in the twist and bend measurements were 4, 2, and 0.1 cm, respectively.

Human Motion Sensing: For human motion monitoring, the the CH Instruments Model 700E was used. Samples for finger and wrist motion were 3 cm long, and samples for knee, elbow, and shoulder motion were 7 cm long. Informed consent was obtained from the volunteer (Xin Wang) for the motion sensing experiments.

Supporting Information

Supporting Information is available from the Wiley Online Library or from the author.

Acknowledgements

This work was partially supported by the National Natural Science Foundation of China (grant no. 61925304). The research work was financially supported by the Hong Kong Research Grants Council (RGC) with project Nos. JLF5/E-402/18 and E-CUHK401/20, the RGC Collaborative Research Fund (CRF) with Project Nos. C4063-18GF and C1134-20GF; the ITF project with Project Nos. MRP/036/18X and ITS/374/18FP funded by the HKSAR Innovation and Technology Commission (ITC); the Croucher Foundation Grant with Ref. No. CAS20403, and the CUHK internal grants. The authors also thank the SIAT-CUHK Joint Laboratory of Robotics and Intelligent Systems.

Conflict of Interest

The authors declare no conflict of interest.

Author Contributions

M.S. conceived and designed the processing approach. M.S. conducted the experiments and wrote the manuscript with input from the other authors. M.S. and X.W. co-analyzed the experimental and calculated data. B.H. completed the simulation of slime deformation. H.X. and L.Z. mentored the work and revised the manuscript. All authors wrote the paper.

Data Availability Statement

The data that support the findings of this study are available from the corresponding author upon reasonable request.

Keywords

circuit control, environmental adaptability, large deformation, magnetic slime, manipulation, self-healing

Received: December 7, 2021

Revised: March 12, 2022

Published online: March 25, 2022

- [1] V. K. Bandari, Y. Nan, D. Karnaushenko, Y. Hong, B. Sun, F. Striggow, D. D. Karnaushenko, C. Becker, M. Faghieh, M. Medina-Sánchez, O. G. Schmidt, *Nat. Electron.* **2020**, 3, 172.
- [2] Y. Zhao, C. Xuan, X. Qian, Y. Alsaïd, M. Hua, L. Jin, X. He, *Sci. Rob.* **2019**, 4, eaax7112.
- [3] X. Qian, Y. Zhao, Y. Alsaïd, X. Wang, M. Hua, T. Galy, H. Gopalakrishna, Y. Yang, J. Cui, N. Liu, M. Marszewski, L. Pilon, H. Jiang, X. He, *Nat. Nanotechnol.* **2019**, 14, 1048.
- [4] S. Tang, F. Zhang, H. Gong, F. Wei, J. Zhuang, E. Karshalev, B. Esteban-Fernández de Ávila, C. Huang, Z. Zhou, Z. Li, L. Yin, H. Dong, R. H. Fang, X. Zhang, L. Zhang, J. Wang, *Sci. Rob.* **2020**, 5, eaba6137.
- [5] W. Gao, S. Sattayasamitsathit, K. M. Manesh, D. Weihs, J. Wang, *J. Am. Chem. Soc.* **2010**, 132, 14403.
- [6] B. Wang, K. F. Chan, K. Yuan, Q. Wang, X. Xia, L. Yang, H. Ko, Y. X. J. Wang, J. J. Y. Sung, P. W. Y. Chiu, L. Zhang, *Sci. Rob.* **2021**, 6, eabd2813.
- [7] J. Wang, W. Gao, *ACS Nano* **2012**, 6, 5745.
- [8] S. Fusco, M. S. Sakar, S. Kennedy, C. Peters, R. Bottani, F. Starsich, A. Mao, G. A. Sotiriou, S. Pané, S. E. Pratsinis, D. Mooney, B. J. Nelson, *Adv. Mater.* **2014**, 26, 952.
- [9] K. E. Peyer, L. Zhang, B. J. Nelson, *Nanoscale* **2013**, 5, 1259.
- [10] J. Li, B. Esteban-Fernández de Ávila, W. Gao, L. Zhang, J. Wang, *Sci. Rob.* **2017**, 2, eaam6431.
- [11] X. Wang, X. H. Qin, C. Hu, A. Terzopoulou, X. Z. Chen, T. Y. Huang, K. Maniura-Weber, S. Pané, B. J. Nelson, *Adv. Funct. Mater.* **2018**, 28, 1804107.
- [12] B. Wang, K. Kostarelos, B. J. Nelson, L. Zhang, *Adv. Mater.* **2021**, 33, 2002047.
- [13] M. Sun, X. Fan, X. Meng, J. Song, W. Chen, L. Sun, H. Xie, *Nanoscale* **2019**, 11, 18382.
- [14] D. Jin, K. Yuan, X. Du, Q. Wang, S. Wang, L. Zhang, *Adv. Mater.* **2021**, 33, 2100070.
- [15] T. G. Leong, C. L. Randall, B. R. Benson, N. Bassik, G. M. Stern, D. H. Gracias, *Proc. Natl. Acad. Sci. USA* **2009**, 106, 703.
- [16] J. Li, X. Li, T. Luo, R. Wang, C. Liu, S. Chen, D. Li, J. Yue, S.-H. Cheng, D. Sun, *Sci. Rob.* **2018**, 3, eaat8829.
- [17] S. Jeon, S. Kim, S. Ha, S. Lee, E. Kim, S. Y. Kim, S. W. Park, J. H. Jeon, S. W. Kim, C. Moon, B. J. Nelson, J. Y. Kim, S. W. Yu, H. Choi, *Sci. Rob.* **2019**, 4, eaav4317.
- [18] Y. Dong, L. Wang, N. Xia, Y. Wang, S. Wang, Z. Yang, D. Jin, X. Du, E. Yu, C. Pan, B. Liu, L. Zhang, *Nano Energy* **2021**, 88, 106254.
- [19] J. Yu, D. Jin, K. F. Chan, Q. Wang, K. Yuan, L. Zhang, *Nat. Commun.* **2019**, 10, 5631.
- [20] J. Yu, B. Wang, X. Du, Q. Wang, L. Zhang, *Nat. Commun.* **2018**, 9, 3260.
- [21] H. Xie, M. M. Sun, X. J. Fan, Z. H. Lin, W. N. Chen, L. Wang, L. X. Dong, Q. He, *Sci. Rob.* **2019**, 4, eaav8006.
- [22] Q. Wang, K. F. Chan, K. Schweizer, X. Du, D. Jin, S. C. H. Yu, B. J. Nelson, L. Zhang, *Sci. Adv.* **2021**, 7, eabe5914.
- [23] M. Sun, X. Fan, C. Tian, M. Yang, L. Sun, H. Xie, *Adv. Funct. Mater.* **2021**, 31, 2011193.
- [24] M. Sun, Q. Liu, X. Fan, Y. Wang, W. Chen, C. Tian, L. Sun, H. Xie, *Small* **2020**, 16, 1906701.
- [25] M. Sun, W. Chen, X. Fan, C. Tian, L. Sun, H. Xie, *Appl. Mater. Today* **2020**, 20, 100682.
- [26] W. Hu, G. Z. Lum, M. Mastrangeli, M. Sitti, *Nature* **2018**, 554, 81.
- [27] T. Xu, J. Zhang, M. Salehizadeh, O. Onaizah, E. Diller, *Sci. Rob.* **2019**, 4, eaav4494.
- [28] X. Du, H. Cui, T. Xu, C. Huang, Y. Wang, Q. Zhao, Y. Xu, X. Wu, *Adv. Funct. Mater.* **2020**, 30, 1909202.
- [29] X. Kuang, S. Wu, Q. Ze, L. Yue, Y. Jin, S. M. Montgomery, F. Yang, H. J. Qi, R. Zhao, *Adv. Mater.* **2021**, 33, 2102113.
- [30] T. Wang, Z. Ren, W. Hu, M. Li, M. Sitti, *Sci. Adv.* **2021**, 7, eabf7364.
- [31] H. Lu, M. Zhang, Y. Yang, Q. Huang, T. Fukuda, Z. Wang, Y. Shen, *Nat. Commun.* **2018**, 9, 3944.
- [32] Y. Cheng, K. H. Chan, X. Q. Wang, T. Ding, T. Li, C. Zhang, W. Lu, Y. Zhou, G. W. Ho, *Adv. Funct. Mater.* **2021**, 31, 2101825.
- [33] J. Zhang, Z. Ren, W. Hu, R. H. Soon, I. C. Yasa, Z. Liu, M. Sitti, *Sci. Rob.* **2021**, 6, eabf0112.
- [34] Y. Kim, G. A. Parada, S. Liu, X. Zhao, *Sci. Rob.* **2019**, 4, eaax7329.
- [35] H.-W. Huang, M. S. Sakar, A. J. Petruska, S. Pané, B. J. Nelson, *Nat. Commun.* **2016**, 7, 12263.
- [36] J. D. Carlson, M. R. Jolly, *Mechatronics* **2000**, 10, 555.
- [37] A. G. Olabi, A. Grunwald, *Mater. Design* **2007**, 28, 2658.
- [38] J. Kim, S. E. Chung, S. E. Choi, H. Lee, J. Kim, S. Kwon, *Nat. Mater.* **2011**, 10, 747.
- [39] M. Zrinyi, L. Barsi, A. Büki, *Polym. Gels Networks* **1997**, 5, 415.
- [40] R. Fuhrer, C. M. Schumacher, M. Zeltner, W. J. Stark, *Adv. Funct. Mater.* **2013**, 23, 3845.
- [41] V. Q. Nguyen, A. S. Ahmed, R. V. Ramanujan, *Adv. Mater.* **2012**, 24, 4041.
- [42] G. Z. Lum, Z. Ye, X. Dong, H. Marvi, O. Erin, W. Hu, M. Sitti, *Proc. Natl. Acad. Sci. USA* **2016**, 113, E6007.
- [43] Y. Kim, H. Yuk, R. Zhao, S. A. Chester, X. Zhao, *Nature* **2018**, 558, 274.
- [44] J. Čejková, T. Banno, M. M. Hanczyc, F. Štěpánek, *Artif. Life* **2017**, 23, 528.
- [45] X. Wang, R. Guo, J. Liu, *Adv. Mater. Technol.* **2019**, 4, 1800549.
- [46] F. Li, J. Shu, L. Zhang, N. Yang, J. Xie, X. Li, L. Cheng, S. Kuang, S.-Y. Tang, S. Zhang, W. Li, L. Sun, D. Sun, *Appl. Mater. Today* **2020**, 19, 100597.
- [47] S. Chen, H.-Z. Wang, R.-Q. Zhao, W. Rao, J. Liu, *Matter* **2020**, 2, 1446.
- [48] X. Zhang, L. Sun, Y. Yu, Y. Zhao, *Adv. Mater.* **2019**, 31, 1903497.
- [49] W. Yu, H. Lin, Y. Wang, X. He, N. Chen, K. Sun, D. Lo, B. Cheng, C. Yeung, J. Tan, D. Di Carlo, S. Emaminejad, *Sci. Rob.* **2020**, 5, eaba4411.
- [50] M. Zhou, Z. Wu, Y. Zhao, Q. Yang, W. Ling, Y. Li, H. Xu, C. Wang, X. Huang, *Adv. Sci.* **2019**, 6, 1901862.
- [51] F. Serwane, A. Mongera, P. Rowghanian, D. A. Kealhofer, A. A. Lucio, Z. M. Hockenbery, O. Campas, *Nat. Methods* **2017**, 14, 181.
- [52] A. Mongera, P. Rowghanian, H. J. Gustafson, E. Shelton, D. A. Kealhofer, E. K. Carn, F. Serwane, A. A. Lucio, J. Giammona, O. Campás, *Nature* **2018**, 561, 401.
- [53] X. Fan, X. Dong, A. Karacakol, H. Xie, M. Sitti, *Proc. Natl. Acad. Sci. USA* **2020**, 117, 27916.

- [54] L. Hu, H. Wang, X. Wang, X. Liu, J. Guo, J. Liu, *ACS Appl. Mater. Interfaces* **2019**, *11*, 8685.
- [55] F. Li, S. Kuang, X. Li, J. Shu, W. Li, S.-Y. Tang, S. Zhang, *Adv. Mater. Technol.* **2019**, *4*, 1800694.
- [56] X. Li, S. Li, Y. Lu, M. Liu, F. Li, H. Yang, S.-Y. Tang, S. Zhang, W. Li, L. Sun, *ACS Appl. Mater. Interfaces* **2020**, *12*, 37670.
- [57] G. Cai, J. Wang, K. Qian, J. Chen, S. Li, P. S. Lee, *Adv. Sci.* **2017**, *4*, 1600190.
- [58] M. Karolina Pierchala, F. B. Kadumudi, M. Mehrli, T. G. Zsurzan, P. J. Kempen, M. P. Serdeczny, J. Spangenberg, T. L. Andresen, A. Dolatshahi-Pirouz, *ACS Nano* **2021**, *15*, 9531.
- [59] W. Stöber, A. Fink, E. Bohn, *J. Colloid Inter. Sci.* **1968**, *26*, 62.